Investigation into the effect of Si doping on the performance of SrFeO$_{3-\delta}$ SOFC electrode materials†

Jose M. Porras-Vazquez,*[a] Thomas Pike,[a] Cathryn A. Hancock,[a] Jose F. Marco,[b] Frank J. Berry[a] and Peter R. Slater*[a]

In this paper we report the successful incorporation of silicon into SrFeO$_{3-\delta}$ perovskite materials for potential applications as electrode materials for solid oxide fuel cells. It is observed that Si doping leads to a change from a tetragonal cell (with partial ordering of oxygen vacancies) to a cubic one (with the oxygen vacancies disordered). Annealing experiments in 5% H$_2$/95% N$_2$ (up to 800 °C) also showed the stabilization of the cubic form for the Si-doped samples under reducing conditions, suggesting that they may be suitable for both cathode and anode applications. In contrast to the cubic cell of the reduced Si doped system, reduction of undoped SrFeO$_{3-\delta}$ leads to the formation of a brownmillerite structure with ordered oxide ion vacancies. SrFe$_{0.90}$Si$_{0.10}$O$_{3-\delta}$ and SrFe$_{0.85}$Si$_{0.15}$O$_{3-\delta}$ were analysed by neutron powder diffraction, and the data confirmed the cubic cell, with no long range oxygen vacancy ordering. Mössbauer spectroscopy data were also recorded for SrFe$_{0.90}$Si$_{0.10}$O$_{3-\delta}$, and indicated the presence of only Fe^{3+} and Fe^{5+} (*i.e.* disproportionation of Fe^{4+} to Fe^{3+} and Fe^{5+}) for such doped samples. Conductivity measurements showed an improvement in the conductivity on Si doping. Composite electrodes with 50% Ce$_{0.9}$Gd$_{0.1}$O$_{1.95}$ were therefore examined on dense Ce$_{0.9}$Gd$_{0.1}$O$_{1.95}$ pellets in two different atmospheres: air and 5% H$_2$/95% N$_2$. In both atmospheres an improvement in the area specific resistance (ASR) values is observed for the Si-doped samples. Thus the results show that silicon can be incorporated into SrFeO$_{3-\delta}$-based materials and can have a beneficial effect on the performance, making them potentially suitable for use as cathode and anode materials in symmetrical SOFCs.

1 Introduction

Perovskite transition metal containing oxides have attracted considerable interest due to potential applications as cathode materials in the field of Solid Oxide Fuel Cells (SOFCs). Traditionally doping strategies for such materials have focused on substitution with cations of similar size, *e.g.* Sr for La.[1–5] In addition, perovskite-type anodes, such as Sr$_{1-x}$Ti$_{1-2x}$Nb$_{2x}$O$_3$, La$_{0.75}$Sr$_{0.25}$Cr$_{0.5}$Mn$_{0.5}$O$_{3-\delta}$, La$_4$Sr$_8$Ti$_{11}$Mn$_{0.5}$Ga$_{0.5}$O$_{37.5-\delta}$ and Sr$_2$MgMoO$_6$, have also been investigated in recent years as alternatives to Ni-cermets to allow the direct utilization of commercial hydrocarbon fuels (with their associated impurities, *e.g.* S).[6–11]

Perovskite SrFeO$_{3-\delta}$ is an interesting material which exhibits high mixed oxide ionic and electronic conductivity and therefore can be potentially used in electrochemical devices such as oxygen permeation membranes, oxygen sensors, and SOFCs.[12–14] Iron cations in this system are in a mixed valence state ranging from

+4 to +3, corresponding to a wide range of oxygen non-stoichiometry, while the structure changes from tetragonal to orthorhombic brownmillerite type, as the iron oxidation state reduces to 3+ and hence the composition changes to SrFeO$_{2.5}$, with associated long range ordering of oxide ion vacancies.[15–17] The formation of ordered oxygen vacancies is not favourable for practical applications because it drastically reduces oxide ion conduction, while the oxygen deficiency also results in a decrease in both mobility and concentration of hole carriers.[18,19] Therefore, in this work we propose the modifications of SrFeO$_3$-based materials through the incorporation of silicate to stabilize the high symmetry cubic form, even at low oxygen partial pressures.

The approach employed stems from prior observations on the successful incorporation of oxyanions into perovskite-type cuprate superconductors and related phases.[20–28] This work demonstrated that the perovskite structure can incorporate significant levels of oxyanions (carbonate, borate, nitrate, sulfate, and phosphate). In such samples, C, B, N, P, and S of the oxyanion group were shown to reside on the perovskite B cation site, with the oxide ions of this group filling 3 (C, B, N) – 4 (P, S) of the available 6 oxide ion positions around this site.

Recently we have illustrated this oxyanion doping strategy in perovskite-type materials with potential for use in solid oxide fuel cells.[29–31] For instance, borate, phosphate and sulphate

[a]School of Chemistry, University of Birmingham, Birmingham, B15 2TT, UK. E-mail: p.r.slater@bham.ac.uk; j.m.porras@bham.ac.uk; Fax: +44 (0)1214144403; Tel: +44 (0)1214148672

[b]Instituto de Química Física "Rocasolano", CSIC, Serrano 119, 28006, Madrid, Spain
† Electronic supplementary information (ESI) available. See DOI: 10.1039/c3ta12113e

were successfully incorporated into different cathode materials such as $SrCoO_{3-\delta}$, $La_{1-x}Sr_xCo_{0.8}Fe_{0.2}O_{3-\delta}$, $Ba_{1-x}Sr_xCo_{0.8}Fe_{0.2}O_{3-\delta}$, $CaMnO_3$ and $La_{1-x}Sr_xMnO_3$-type materials, leading to stabilization of high symmetry forms, enhancements in the electronic conductivity, as well as the electrode performance, with respect to the parent compounds.

The introduction of silicate groups is of particular interest, since silica is widely considered a detrimental contaminant of SOFC materials, particularly electrolyte materials, as it has been reported to segregate at the grain boundaries where it forms insulating siliceous phases, lowering the conductivity, such that overall performance is degraded.[32–38] For example, it has been reported that several hundreds of ppm of SiO_2 can increase the electrolyte grain boundary resistance by over one order of magnitude.[39–41]

Our preliminary studies on Si incorporation were performed in cobalt-based perovskite electrode materials, showing the successful incorporation of Si into $La_{0.6}Sr_{0.4}Co_{0.8}Fe_{0.2}O_{3-\delta}$ and $Sr_{1-x}Y_xCoO_{3-\delta}$-based materials, with significant results in terms of improvements in the conductivity and an enhancement in the stability towards CO_2.[42] The enhancement in performance is in contrast to previous assumptions of the detrimental effect of Si and can be attributed to the incorporation of the Si into the perovskite structure, whereas in prior studies of the effect of Si on fuel cell materials researchers have typically examined its addition as a secondary phase. Very recently, $Sr_yCa_{1-y}Mn_{1-x}Si_xO_{3-\delta}$ cathode materials have been prepared by solid state reaction, and direct evidence for the incorporation of Si into the structure is provided for the first time by ^{29}Si NMR.[43,44] In each case, Si doping is shown to enhance the conductivity, which can be attributed to electron doping (driven by the introduction of oxide ion vacancies due to the preference for Si to adopt tetrahedral coordination), as well as, for some systems, a change from a hexagonal (containing face sharing of octahedra) to a cubic perovskite (containing corner sharing of octahedra).

Therefore, in this work we have extended these studies to silicon doping into $SrFeO_{3-\delta}$ systems, with a view to stabilize the cubic form of these systems at low oxygen partial pressures, avoiding its transition to the brownmillerite form, and thus, potentially allowing the use of these samples as anode and cathode materials in symmetrical fuel cells. In addition Si and Fe containing perovskites are of interest in Earth Science, where (Mg, Fe)SiO_3, (Ca, Fe)SiO_3 and Ca(Si, Fe)O_{3-x} phases have attracted substantial interest due to their accepted presence in the Earth's interior.[45–48] Such phases have been traditionally thought to require very high pressure synthesis conditions, and so the work here, showing for the first time synthesis of an Fe and Si containing perovskite at ambient pressure, is of significant relevance to a perovskite chemistry field in general.

2 Experimental

$SrCO_3$ (Aldrich, 99.9%), Fe_2O_3 (Fluka, 99%) and SiO_2 (Aldrich, 99.6%) were used to prepare $SrFe_{1-x}Si_xO_{3-\delta}$ ($x \leq 0.15$). The powders were intimately ground and heated initially to 1100 °C for 12 h. They were then ball-milled (350 rpm for 1 hour, Fritsch

Pulverisette 7 Planetary Mill) and reheated to 1150 °C for a further 12 h. Finally, they were then ball-milled (350 rpm for 1 hour) and reheated to 1200 °C for a further 12 h. All the heating processes were carried out in air.

Powder X-ray diffraction (XRD) (Bruker D8 diffractometer with Cu $K\alpha_1$ radiation in transmission mode, Debye–Scherrer) was used to demonstrate phase purity, as well as for cell parameter determination. For the latter, the GSAS suite of programs was used.[49] In order to obtain further structural details, neutron diffraction data were collected on an HRPT diffractometer[50] [SINQ neutron source at Paul Scherrer Institut, Villigen, Switzerland]. Rietveld refinement was performed using the GSAS suite of programs.[49] Oxygen contents were estimated from thermogravimetric analysis (Netzsch STA 449 F1 Jupiter Thermal Analyser). Samples were heated at 10 °C min^{-1} to 1200 °C in N_2 and held for 30 minutes to reduce the Fe oxidation state to 3+, with the original oxygen content and average Fe oxidation state then being determined from the mass loss observed.

To determine the potential use of these materials as SOFC anodes the samples were annealed for 24 hours at 800 °C in 5% H_2–95% Ar to study the effect of silicon doping on the stability under reducing conditions.

In order to gather further information on the Fe oxidation state, ^{57}Fe Mössbauer spectra were recorded in constant acceleration mode using a *ca.* 25 mCi^{57}Co/Rh source and a helium closed-cycle cryo-refrigerator. All the spectra were computer fitted and the chemical isomer shift data are quoted relative to metallic iron at 298 K.

Pellets for conductivity measurements were prepared as follows: the powders were first ball-milled (350 rpm for 1 hour), before pressing (200 MPa) as pellets and sintering at 1200 °C for 12 h. Four Pt electrodes were attached with Pt paste, and then the sample was fired to 800 °C in air for 1 hour to ensure bonding to the sample. The samples were then furnace cooled to 350 °C in air and held at this temperature for 12 hours to ensure full oxygenation. Conductivities were then measured using the four probe dc method in two different atmospheres: air (for cathode applications) and 5% H_2/95% N_2 (for anode applications).

To elucidate the potential of these materials as SOFC electrodes, symmetrical electrodes were coated on both sides of dense $Ce_{0.9}Gd_{0.1}O_{1.95}$ (CGO10, Aldrich) pellets (sintered at 1500 °C for 12 h) using a suspension prepared with a mixture of electrolyte and electrodes (1 : 1 wt%) and Decoflux™ (WB41, Zschimmer and Schwarz) as a binder material. The symmetrical cells were fired at 900 °C for 1 h in air. Afterwards, a Pt-based ink was applied onto the electrodes to obtain a current collector layer and finally fired at 800 °C for 1 hour. Area-specific resistance (ASR) values were then obtained under both symmetrical air (cathodic conditions) and 5% H_2/95% N_2 (anodic conditions) atmospheres in a two electrode configuration. To avoid the reduction of the CGO electrolyte, the measurements were carried out only at 600 °C under reducing conditions. Impedance spectra of the electrochemical cells were collected using a HP4912A frequency analyser, at open circuit voltage (OCV), in the 5 Hz to 13 MHz frequency range with an ac signal amplitude of 100 mV. The spectra were fitted to equivalent

This journal is © The Royal Society of Chemistry 2013

J. Mater. Chem. A, 2013, **1**, 11834–11841 | **11835**

circuits using the ZView software[51] which allows an estimation of the resistance and capacitance associated with different cell contributions.
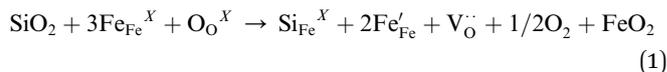
3 Results and discussion

Solid solution range

For the $SrFe_{1-x}Si_xO_{3-\delta}$ series, single phase samples could be achieved up to higher levels of silicon, $x \leq 0.15$. Exceeding this Si content led to the segregation of secondary phases, such as Sr_2SiO_4 (PDF 038-0271). The undoped sample showed a tetragonal symmetry due to partial ordering of the oxygen vacancies. This is clearly seen in the inset of Fig. 1, where we can observe the splitting of the peaks in the 45–60 2θ (°) region. Through Si doping there was no long range oxygen ordering and the samples showed a cubic cell, see Fig. 1.

Cell parameters for these systems were determined from the X-ray diffraction data using the Rietveld method (see Table 1), showing an increase in the cell volume as the Si content increases. The Rietveld plots for $SrFeO_{3-\delta}$ and $SrFe_{0.9}Si_{0.1}O_{3-\delta}$ are shown in Fig. S1.† In addition, hkl values for the main diffraction peaks are shown in Tables S1 and S2† for $SrFeO_{3-\delta}$ and $SrFe_{0.9}Si_{0.1}O_{3-\delta}$. Similar results were reported in a previous study where (Ca, Sr)MnO₃-based compounds were successfully doped with silicon.[44] The change in cell parameters for these oxyanion doped perovskite materials is a balance between the effect of the smaller size of Si^{4+} ions, which would be expected to lead to a reduction in cell volume, and the associated reduction of Fe^{4+} to give a higher concentration of Fe^{3+}, which would be expected to lead to an increase in cell volume. The formation of 3+ species through Si doping is predicted by the following defect equation:

Table 1 Cell parameters and normalised cell volumes for $SrFe_{1-x}Si_xO_{3-\delta}$ ($x \leq 0.15$) obtained from XRD data analysis. The structure of $SrFeO_{3-\delta}$ was refined in a tetragonal space group ($I4/mmm$). The structures of the doped samples were refined in a cubic space group ($Pm3m$)

$SrFe_{1-x}Si_xO_{3-\delta}$				
Si (x)	0	0.05	0.10	0.15
a (Å)	10.9235(1)	3.8636(1)	3.8723(1)	3.8755(1)
c (Å)	7.6965(1)	—	—	—
V/Z (Å³)	57.40(1)	57.67(1)	58.06(1)	58.34(1)
R_{wp} (%)	3.43	3.08	2.82	2.66

$$SiO_2 + 3Fe_{Fe}^{X} + O_{O}^{X} \rightarrow Si_{Fe}^{X} + 2Fe'_{Fe} + V_{O}^{\cdot\cdot} + 1/2O_2 + FeO_2 \quad (1)$$

As can be seen from the above equation, a key driving force for the reduction of Fe^{4+} to Fe^{3+} is the introduction of oxide ion vacancies due to the lower coordination (tetrahedral rather than octahedral) preference of the Si dopant (*i.e.* for $x = 0$, the B cation site is completely occupied by Fe, while for $x > 0$ some Si is on this site, which is tetrahedrally coordinated, and thus leads to a reduction in the total oxygen content). Thus, while we are nominally performing an isovalent (Si^{4+} in place of Fe^{4+}) substitution, the generation of oxide ion vacancies results in partial reduction, *i.e.* electron doping.

The average oxidation states of Fe in these systems reported in Table 3 showed a decrease in the average iron oxidation state and increase in the oxygen vacancies as the Si content increases, in good agreement with the defect equation given above illustrating the predicted effect of Si-doping in these systems.

Keeping in mind the use of these materials in symmetrical fuel cells, their stability was also examined under reducing conditions (24 h at 800 °C in 5% H_2–95% N_2), to examine their possible application as SOFC anode materials. The undoped sample, $SrFeO_{3-\delta}$, showed a transition from a tetragonal to an orthorhombic symmetry (see Fig. 2). This behaviour is due to the loss of oxygen, leading to the formation of a phase ($Sr_2Fe_2O_5$) with the brownmillerite structure and ordered oxygen vacancies. On Si-doping we see a stabilization of the cubic symmetry under reducing conditions for silicon contents higher than or equal to $x = 0.10$. Therefore, through silicon doping we have achieved the stabilisation of the high symmetry form under reducing conditions, which is likely to help maintain its electrical properties and avoid anisotropic changes of dimensions that may provoke a mechanical failure in the working cell.

Neutron diffraction structural study

The structures of the $SrFe_{1-x}Si_xO_{3-\delta}$ series, $x = 0.1$ and 0.15, samples were examined using neutron diffraction data. The data indicated a cubic cell ($Pm\bar{3}m$), with no evidence for the presence of extra peaks indicative of oxide vacancy ordering (see Fig. 3 and 4). The R factors were very low, $R_{wp} = 3.73\%$ and $R_F = 1.17\%$ for $SrFe_{0.9}Si_{0.1}O_{3-\delta}$ and $R_{wp} = 3.47\%$ and $R_F = 1.31\%$ for $SrFe_{0.85}Si_{0.15}O_{3-\delta}$, indicating a good fit to the data. The refined structural data are shown in Table 2. The usual parameters: histogram scale factors, background coefficients, unit cell
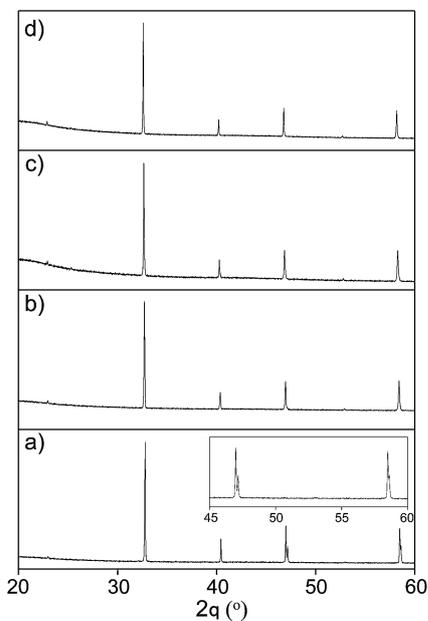

Fig. 1 X-ray diffraction patterns of (a) $SrFeO_{3-\delta}$, (b) $SrFe_{0.95}Si_{0.05}O_{3-\delta}$, (c) $SrFe_{0.90}Si_{0.10}O_{3-\delta}$ and (d) $SrFe_{0.85}Si_{0.15}O_{3-\delta}$. The inset shows the expanded region from 45 to 60° 2θ for $SrFeO_{3-\delta}$.
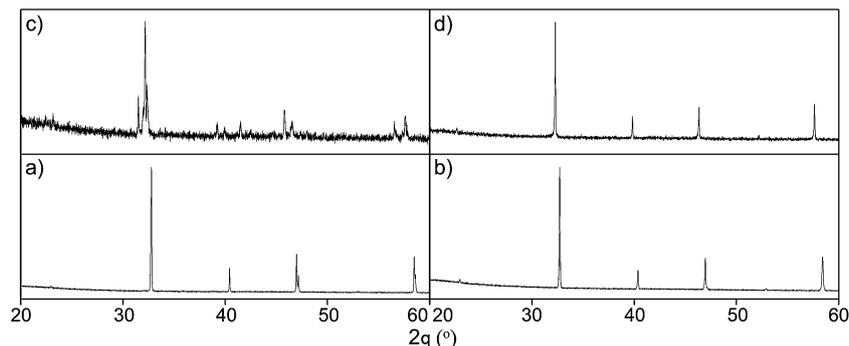
Fig. 2 X-ray diffraction patterns of (a) $SrFeO_{3-\delta}$ and (b) $SrFe_{0.90}Si_{0.10}O_{3-\delta}$, as prepared; and (c) $SrFeO_{3-\delta}$ and (d) $SrFe_{0.90}Si_{0.10}O_{3-\delta}$, annealed at 800 °C for 24 h in 5% H_2–95% N_2.

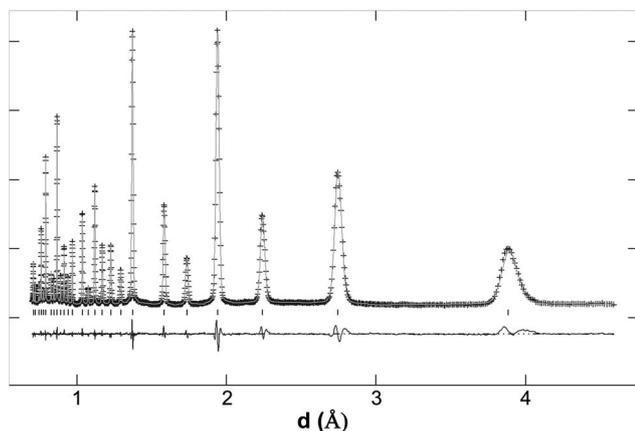**Fig. 3** Observed, calculated and difference neutron diffraction profiles of $SrFe_{0.90}Si_{0.10}O_{3-\delta}$. The structure was refined in a cubic space group ($Pm\bar{3}m$).
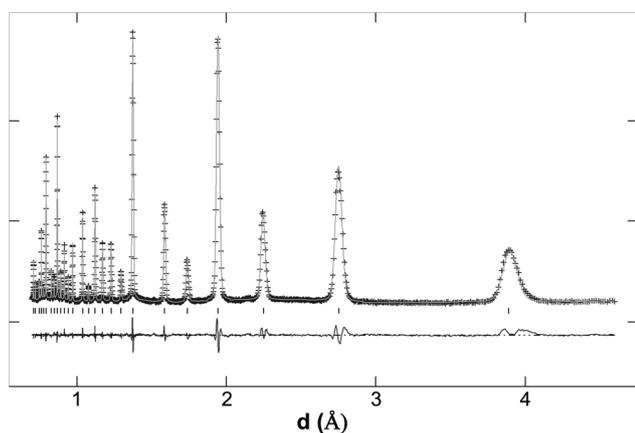

Fig. 4 Observed, calculated and difference neutron diffraction profiles of $SrFe_{0.85}Si_{0.15}O_{3-\delta}$. The structure was refined in a cubic space group ($Pm\bar{3}m$).

Table 2 Atomic positions and structural parameters obtained from neutron powder diffraction data for $SrFe_{1-x}Si_xO_{3-\delta}$ ($x = 0.10$ and 0.15). The structures were refined in a cubic space group ($Pm\bar{3}m$)

Atom (x, y, z)	$x = 0.10$		$x = 0.15$	
	100 UISO	Occupancy	100 UISO	Occupancy
Sr (0.5, 0.5, 0.5)	1.07(1)	1(–)	1.22(1)	1(–)
Fe (0, 0, 0)	0.77(1)	0.93(1)	0.94(1)	0.88(1)
Si (0, 0, 0)	0.77(1)	0.07(1)	0.94(1)	0.12(1)
O (0.5, 0, 0)	1.65(1)	0.90(1)	1.75(1)	0.87(1)

Table 3 Oxygen deficiencies (δ) and average Fe oxidation states (from TGA), and conductivity data at 700 °C and ASR values at 800 °C in air for the $SrFe_{1-x}Si_xO_{3-\delta}$ series. The errors estimated for the oxygen deficiencies and iron oxidation states from the TGA data are ± 0.01 and ± 0.02 respectively

$SrFe_{1-x}Si_xO_{3-\delta}$				
Si (x)	0	0.05	0.10	0.15
Oxygen deficiency (δ)	0.10	0.20	0.23	0.25
Oxidation state	3.80	3.60	3.48	3.42
Conductivity at 700 °C (S cm^{-1})	26.3	21.2	35.3	17.8
Conductivity at 800 °C (S cm^{-1})	17.2	14.6	24.1	13.4
ASR at 700 °C (Ω cm^2)	1.65	1.19	0.90	1.88
ASR at 800 °C (Ω cm^2)	0.25	0.14	0.08	0.28

from the starting composition. Atomic displacement parameters were refined as isotropic. As can be seen from Table 2 the oxygen atomic displacement parameters are higher than the other atoms which can be related to the local distortions caused by the presence of the silicate groups. The data confirm the importance of silicon doping in these strontium ferrites showing the stabilization of the cubic form, with no long range oxide vacancy ordering. As future work, we are planning to carry out total scattering experiments to study the local structure of these samples and the effect of the introduction of a silicate group.

^{57}Fe Mössbauer spectroscopy

^{57}Fe Mössbauer data were collected in order to gain further information on the oxidation state and environment of iron.

parameters, zero error and peak shape coefficients were varied. For the refinement, the atomic displacement parameters for Fe and Si were constrained to be equal. The Fe and Si occupancies were refined, with the constraint that their sum equalled 1.0, and the final values were in good agreement with those expected

The spectra recorded from $SrFe_{0.9}Si_{0.1}O_{3-\delta}$ at 298 K showed three quadrupole split absorptions (Fig. 5). The doublet with a chemical isomer shift of $\delta \approx -0.05$ mm s^{-1} can be associated with Fe^{5+} in perovskite-related structures.[52–54] The component with chemical isomer shift $\delta \approx 0.37$ is typical of Fe^{3+} in octahedral coordination[55] whilst the doublet with chemical isomer shift $\delta \approx 0.18$ mm s^{-1} is indicative of Fe^{3+} in a lower coordination[55] (see Table 5). The results demonstrate that substitution of Fe^{4+} in $SrFeO_{3-\delta}$ by Si^{4+} induces disproportionation of the remaining Fe^{4+} into Fe^{3+} and Fe^{5+}. This has previously been observed by substituting the larger Sn^{4+} ions in place of Fe^{4+} ions in $SrFeO_{3-\delta}$, which causes lattice strain that can be mitigated by incorporating smaller Fe^{5+} ions.[56,57] In this case the situation is most likely reversed with the smaller Si^{4+} ions causing significant local strain resulting in the Si^{4+} being surrounded by the large Fe^{3+} ions to relieve the strain with the adjacent cells incorporating the smaller Fe^{5+} ions.

The unfitted ^{57}Fe Mössbauer spectra from $SrFe_{0.9}Si_{0.1}O_{3-\delta}$ between 300 and 15 K (Fig. S2†) show that the material becomes magnetically ordered between 68 and 42 K. The spectra recorded from the magnetically ordered materials were complex and their resistance to fitting is consistent with the complexity of the interactions between Fe^{3+} and Fe^{5+} at low temperatures.

The spectra at 298 and 16 K from the H_2 reduced parent material (Fig. 6) were best fitted to three sextets with chemical isomer shifts characteristic of Fe^{3+} (see Table 5). The results show that the reducing conditions cause the conversion of Fe^{5+} to Fe^{3+} resulting in a composition of $SrFe_{0.9}Si_{0.1}O_{2.55}$. As can be seen, the spectra at 16 K for the reduced material are less complex compared to its prereduced counterpart since only Fe^{3+} superexchange interactions were observed, compared to the complex interactions in the prereduced material between the iron in different oxidation states. Previous studies have shown that the reduction of undoped $SrFeO_{3-\delta}$ results in brownmillerite-related $Sr_2Fe_2O_5$ where the oxide ion vacancies are ordered.[58] The ^{57}Fe Mössbauer spectra recorded here from reduced $SrFe_{0.9}Si_{0.1}O_{3-\delta}$ were significantly different from those recorded previously from $Sr_2Fe_2O_5$ which showed two sextets of equal area characteristic of equal amounts of octahedrally and tetrahedrally coordinated Fe^{3+}.[59–61] Attempts to fit our data to two sextets were not satisfactory. This can be explained by the extra oxygen in $SrFe_{0.9}Si_{0.1}O_{2.55}$ ($Sr_2Fe_{1.8}Si_{0.2}O_{5.1}$) leading to disorder on the oxygen sublattice.
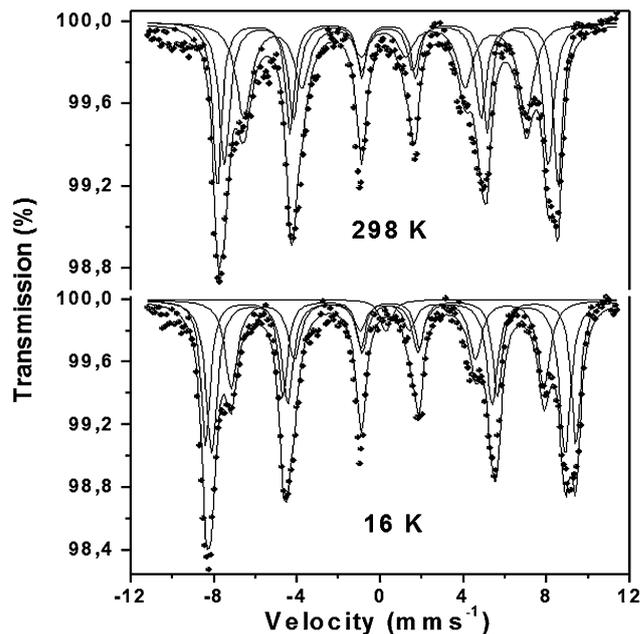

Fig. 6 ^{57}Fe Mössbauer spectra recorded from reduced $SrFe_{0.90}Si_{0.10}O_{3-\delta}$ at 298 and 16 K.

Conductivity measurements

The conductivities of the samples were measured in two different atmospheres: air (for cathode applications) and 5% H_2/95% N_2 (for anode applications).

Air atmosphere

An increase in conductivity was observed for the 10% doped ($x = 0.1$) sample, with further increases in Si content lowering the conductivity (see Fig. 7). The initial increase in conductivity for $x = 0.1$ may result from the observed changes in the Fe oxidation state as well as possibly an improvement in the conduction pathways from the change from a tetragonal to a more symmetrical cubic system. When the doping level
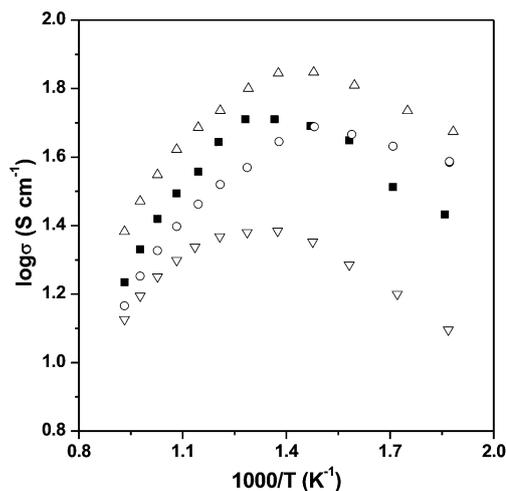

Fig. 5 ^{57}Fe Mössbauer spectrum recorded from $SrFe_{0.90}Si_{0.10}O_{3-\delta}$ at 298 K.

Fig. 7 Plot of log σ vs. 1000/T for $SrFeO_{3-\delta}$ (■), $SrFe_{0.95}Si_{0.05}O_{3-\delta}$ (○), $SrFe_{0.90}Si_{0.10}O_{3-\delta}$ (△) and $SrFe_{0.85}Si_{0.15}O_{3-\delta}$ (▽) in air.

11838 | J. Mater. Chem. A, 2013, **1**, 11834–11841

This journal is © The Royal Society of Chemistry 2013

increases further, the conductivity then decreases due to the silicate disrupting the Fe–O network. All samples showed a decrease in the conductivity above ~400 °C, due to oxygen loss at these higher temperatures reducing the Fe^{4+} content.

5% H₂/95% N₂ atmosphere

Under these conditions we can see an important drop in the conductivity values, with respect to those obtained in air, due to the reduction in the iron oxidation state. The best conductivity values in the $SrFe_{1-x}Si_xO_{3-\delta}$ series were obtained for $x \geq 0.10$ (see Table 4). This behaviour is in good agreement with the fact that, for this series, the $x \leq 0.05$ samples showed a transition to a brownmillerite phase, detrimental to the electrical properties.

Area-specific resistance study

Following the conductivity results, cathode testing was performed for the $SrFe_{1-x}Si_xO_{3-\delta}$ series. These experiments used a composite of the perovskite and CGO10 (1 : 1 wt%) on dense CGO10 pellets. The composite was deposited at 900 °C, and at this temperature there was no evidence of any segregation of secondary phases in perovskite–CGO10 mixtures.

Air atmosphere

The dependences of ASR in air on temperature are shown in Fig. 8 and Table 3. For instance, for $SrFe_{0.95}Si_{0.05}O_{3-\delta}$ and $SrFe_{0.90}Si_{0.10}O_{3-\delta}$, the values obtained at 800 °C were 0.14 and 0.08 Ω cm², respectively. These results entail a significant improvement with respect to the undoped sample: 0.25 Ω cm². For the highest silicon content, $SrFe_{0.85}Si_{0.15}O_{3-\delta}$, there is no improvement, which is likely due to the disruptive effect of silicon on a conducting Fe–O network. We can see that there is a

non-linear behaviour of the ASR data, with a bigger drop in values at higher temperatures. This behaviour is likely due to the fact that these systems show loss of oxygen at high temperature, causing an increase in oxide vacancies and hence a better oxide ion mobility and ASR values.

5% H₂–95% H₂ atmosphere

The dependences of ASR in 5% H₂–95% H₂ at 600 °C are shown in Table 4. For $SrFe_{0.95}Si_{0.05}O_{3-\delta}$, $SrFe_{0.90}Si_{10}O_{3-\delta}$ and $SrFe_{0.85}Si_{0.15}O_{3-\delta}$ the values obtained were 1.51, 0.17 and 0.24 Ω cm², respectively. These results entail a significant improvement with respect to the undoped sample: 1.86 Ω cm². This behaviour is likely due to the effect of silicon stabilising the cubic lattice and hence inhibiting long range oxide ion vacancy ordering, as previously discussed. In comparison, for current state-of-the-art Ni–CGO composites deposited by spray pyrolysis on CGO pellets, values of 0.34 Ω cm² at 600 °C and 0.09 Ω cm² at 550 °C have been reported in the literature,[62,63] very close to the values observed for $SrFe_{0.90}Si_{10}O_{3-\delta}$ and $SrFe_{0.85}Si_{0.15}O_{3-\delta}$ in this work, where further improvements are likely to be possible through additional morphological control. The results therefore
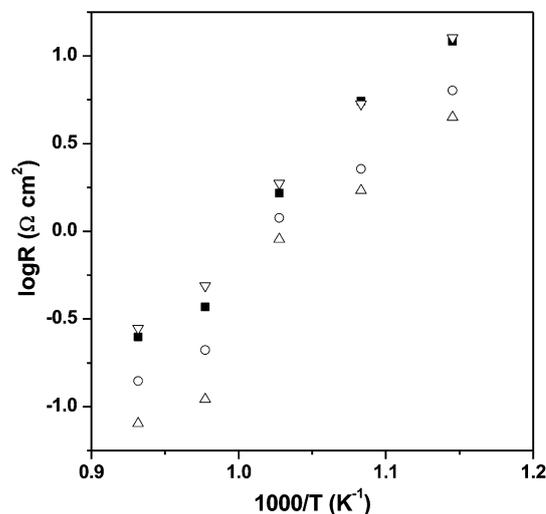
Table 4 Conductivity data at 700 °C and 600 °C, and ASR values at 600 °C in 5% H₂–95% N₂ for the $SrFe_{1-x}Si_xO_{3-\delta}$ series

$SrFe_{1-x}Si_xO_{3-\delta}$				
Si (x)	0	0.05	0.10	0.15
Conductivity at 700 °C (S cm⁻¹)	0.9	0.5	8.3	3.3
Conductivity at 600 °C (S cm⁻¹)	0.6	0.3	5.4	3.0
ASR at 600 °C (Ω cm²)	1.86	1.51	0.17	0.24

Fig. 8 Plot of log(area-specific resistance (ASR)) vs. 1000/T for $SrFeO_{3-\delta}$ (■), $SrFe_{0.95}Si_{0.05}O_{3-\delta}$ (○), $SrFe_{0.90}Si_{0.10}O_{3-\delta}$ (△) and $SrFe_{0.85}Si_{0.15}O_{3-\delta}$ (▽) in air.

Table 5 ⁵⁷Fe Mössbauer parameters obtained from $SrFe_{0.9}Si_{0.1}O_{3-\delta}$

Material	Temperature of measurement (K)	Assignment	$\delta \pm 0.02$ (mm s⁻¹)	Δ or $e^2qQ/2 \pm$ 0.05 (mm s⁻¹)	$H \pm 5$ (T)	Area ± 5 (%)
As-prepared $SrFe_{0.9}Si_{0.1}O_{3-\delta}$	300	Fe^{5+}	−0.05	0.44		34
		Fe^{3+}	0.38	0.65		24
		Fe^{3+}	0.18	0.58		42
	300	Fe^{3+}	0.38	−0.04	51	32
		Fe^{3+}	0.32	−0.04	48	35
		Fe^{3+}	0.19	0.06	42	33
	16	Fe^{3+}	0.49	0.02	55	33
		Fe^{3+}	0.43	−0.08	53	41
		Fe^{3+}	0.29	0.13	47	26

This journal is © The Royal Society of Chemistry 2013

J. Mater. Chem. A, 2013, **1**, 11834–11841 | **11839**

show promising potential for these Si doped perovskites in anode applications, and the fact that these systems are oxides means that problems of C or S poisoning, experienced by Ni containing anodes, may be mitigated in these systems. Further studies are therefore planned to investigate these $SrFe_{1-x}S_xO_{3-\delta}$ anode materials in more detail.

4   Conclusions

$SrFe_{1-x}Si_xO_{3-\delta}$ perovskite materials have been prepared by solid state reaction. A change from tetragonal symmetry (with ordered oxygen vacancies) to cubic (with the oxygen vacancies disordered) is observed through Si doping. Annealing experiments in 5% H_2/95% N_2 showed the stabilization of the cubic form for the Si-doped samples under reducing conditions, making them potentially suitable for anode applications. An improvement in the conductivity is observed on Si doping at the 10% level, although higher levels of Si are shown to decrease the conductivity, which can be attributed to the blocking effect of silicon on the electronic conduction pathways. Composites with 50% $Ce_{0.9}Gd_{0.1}O_{1.95}$ were examined on dense $Ce_{0.9}Gd_{0.1}O_{1.95}$ pellets in two different atmospheres: air and 5% H_2/95% N_2. In both atmospheres an improvement in the area specific resistance (ASR) values is observed for the Si-doped samples. Thus these preliminary results show that silicon can be incorporated into perovskite ferrites and can have a beneficial effect on the performance, making them potentially suitable for use as cathode and anode materials in symmetrical SOFCs. This work also demonstrates for the first time that Fe and Si containing perovskites can be prepared under ambient pressure conditions, contrary to previous studies where it was believed that very high pressures were necessary.

Acknowledgements

References

1 A. Orera and P. R. Slater, *Chem. Mater.*, 2010, **22**, 675.

2 A. J. Jacobson, *Chem. Mater.*, 2010, **22**, 660.

3 A. Lashtabeg and S. J. Skinner, *J. Mater. Chem.*, 2006, **16**, 3161.

4 A. Martínez-Amesti, A. Larranaga, L. M. Rodríguez-Martínez, A. T. Aguayo, J. L. Pizarra, M. L. Nóa, A. Laresgoiti and M. I. Arriortua, *J. Power Sources*, 2008, **185**, 401.

5 D. Kuscer, D. Hanzel, J. Holc, M. Hrovat and D. Kolar, *J. Am. Ceram. Soc.*, 2001, **84**, 1148.

6 J. T. S. Irvine, P. R. Slater and P. A. Wright, *Ionics*, 1996, **2**, 213.

7 P. R. Slater, D. P. Fagg and J. T. S. Irvine, *J. Mater. Chem.*, 1997, **7**, 2495.

8 S. Tao and J. T. S. Irvine, *Nat. Mater.*, 2003, **2**, 320.

9 J. C. Ruiz-Morales, J. Canales-Vázquez, C. Savaniu, D. Marrero-López, W. Zhou and J. T. S. Irvine, *Nature*, 2006, **439**, 568.

10 Y. H. Huang, R. I. Dass, Z. L. Xing and J. B. Goodenough, *Science*, 2006, **312**, 254.

11 Y. H. Huang, R. I. Dass, J. C. Denyszyn and J. B. Goodenough, *J. Electrochem. Soc.*, 2006, **153**, A1266.

12 J. Yoo, A. Verma, S. Wang and A. J. Jacobson, *J. Electrochem. Soc.*, 2005, **152**, A497.

13 A. Evdou, V. Zaspalis and L. Nalbandian, *Fuel*, 2010, **89**, 1265.

14 Y. Niu, W. Zhou, J. Sunarso, L. Ge, Z. Zhu and Z. Shao, *J. Mater. Chem.*, 2010, **20**, 9619.

15 J. P. Hodges, S. Short, J. D. Jorgensen, X. Xiong, B. Dabrowski, S. M. Mini and C. W. Kimball, *J. Solid State Chem.*, 2000, **151**, 190.

16 V. Vashuk, L. Kokhanovskii and I. Yushkevich, *Inorg. Mater.*, 2000, **36**, 79.

17 M. V. Patrakeev, I. A. Leonidov, V. L. Kozhevnikov and V. V. Kharton, *Solid State Sci.*, 2004, **6**, 907.

18 P. Adler, A. Lebon, V. Damljanovic, C. Ulrich, C. Bernhard, A. V. Boris, A. Maljuk, C. T. Lin and B. Keimer, *Phys. Rev. B: Condens. Matter Mater. Phys.*, 2006, **73**, 094451.

19 M. Schmidt and S. J. Campbell, *J. Solid State Chem.*, 2001, **156**, 292.

20 C. Greaves and P. R. Slater, *J. Mater. Chem.*, 1991, **1**, 17.

21 C. Greaves and P. R. Slater, *Physica C*, 1991, **175**, 172.

22 P. R. Slater, C. Greaves, M. Slaski and C. M. Muirhead, *Physica C*, 1993, **208**, 193.

23 Y. Miyazaki, H. Yamane, N. Ohnishi, T. Kajitani, K. Hiraga, Y. Mori, S. Funahashi and T. Hirai, *Physica C*, 1992, **198**, 7.

24 A. Maignan, M. Hervieu, C. Michel and B. Raveau, *Physica C*, 1993, **208**, 116.

25 K. Kinoshita and T. Yamada, *Nature*, 1992, **357**, 313.

26 B. Raveau, M. Hervieu, D. Pelloquin, C. Michel and R. Retoux, *Z. Anorg. Allg. Chem.*, 2005, **631**, 1831.

27 D. Pelloquin, M. Hervieu, C. Michel, N. Nguyen and B. Raveau, *J. Solid State Chem.*, 1997, **134**, 395.

28 V. Caignaert, B. Domenges and B. Raveau, *J. Solid State Chem.*, 1995, **120**, 279.

29 C. A. Hancock, R. C. T. Slade, J. R. Varcoe and P. R. Slater, *J. Solid State Chem.*, 2011, **184**, 2972.

30 J. M. Porras-Vazquez and P. R. Slater, *J. Power Sources*, 2012, **209**, 180.

31 J. M. Porras-Vazquez, T. F. Kemp, J. V. Hanna and P. R. Slater, *J. Mater. Chem.*, 2012, **22**, 8287.

32 D. Ivanova, E. M. C. L. G. P. Lima, A. Kovalevsky, F. M. L. Figueiredo, V. V. Kharton and F. M. B. Marques, *Ionics*, 2008, **14**, 349.

33 X. Guo and R. Waser, *Prog. Mater. Sci.*, 2006, **51**, 151.

34 M. J. Verkerk, A. J. A. Winnubst and A. J. Burggraaf, *J. Mater. Sci.*, 1982, **17**, 3113.

35 S. P. S. Badwal and J. Drennan, *J. Mater. Sci.*, 1987, **22**, 3231.

36 M. L. Mecartney, *J. Am. Ceram. Soc.*, 1987, **70**, 54.

37 S. P. S. Badwal and J. Drennan, *J. Mater. Sci.*, 1989, **24**, 88.

38 D. Ivanova, A. Kovalevsky, V. V. Kharton and F. M. B. Marques, *Bol. Soc. Esp. Ceram. Vidrio*, 2008, **47**, 201.

39 B. C. H. Steele, *Solid State Ionics*, 2000, **129**, 95.

40 T. S. Zhang, J. Ma, S. H. Chan, P. Hing and J. A. Kilner, *Solid State Sci.*, 2004, **6**, 565.

41 S. P. S. Badwal, *Solid State Ionics*, 1995, **76**, 67.

42 J. M. Porras-Vazquez and P. R. Slater, *Fuel Cells*, 2012, **12**, 1056.

43 C. A. Hancock and P. R. Slater, *Dalton Trans.*, 2011, **40**, 5599.

44 J. M. Porras-Vazquez, E. R. Losilla, P. J. Keenan, C. A. Hancock, T. F. Kemp, J. V. Hanna and P. R. Slater, *Dalton Trans.*, 2013, **42**, 5421.

45 U. W. Blass, F. Langenhorst, T. Boffa-Ballaran, F. Seifert, D. J. Frost and C. A. McCammon, *Phys. Chem. Miner.*, 2004, **31**, 52.

46 M. Murakami, K. Hirose, K. Kawamura, N. Sata and Y. Ohishi, *Science*, 2004, **304**, 855.

47 A. R. Oganov and S. Ono, *Nature*, 2004, **430**, 445.

48 A. R. Oganov, R. Martonak, A. Laio, P. Raiteri and M. Parrinello, *Nature*, 2005, **438**, 1142.

49 A. C. Larson and R. B. V. Dreele, *General Structure Analysis System (GSAS) program. Rep. No. LA-UR-86748*, Los Alamos National Laboratory, Los Alamos, CA, 1994.

50 P. Fischer, G. Frey, M. Koch, M. Konnecke, V. Pomjakushin, J. Schefer, R. Thut, N. Schlumpf, R. Burge, U. Greuter, S. Bondt and E. Berruyer, *Physica B*, 2000, **146**, 276.

51 D. Johnson, *ZView: A Software Program for IES Analysis, Version 2.8*, Scribner Associates, Inc. Southern Pines, NC, 2008.

52 P. Adler, *J. Solid State Chem.*, 1997, **130**, 129.

53 S. E. Dann, M. T. Weller, D. B. Currie, M. F. Thomas and A. D. Al-Rawas, *J. Mater. Chem.*, 1993, **3**, 1231.

54 G. S. Case, A. L. Hector, W. Levason, R. L. Needs, M. F. Thomas and M. T. Weller, *J. Mater. Chem.*, 1999, **9**, 2821.

55 F. Menil, *J. Phys. Chem.*, 1985, **46**, 763.

56 G. Demazeau, P. Fabritchnyi, L. Founes, S. Darracq, I. A. Presniakov, K. V. Pokholok, V. P. Gorkov and J. Etourneau, *J. Mater. Chem.*, 1995, **5**, 553.

57 F. J. Berry, A. F. Bowfield, F. C. Coomer, D. Jackson, E. A. Moore, P. R. Slater, M. F. Thomas, A. J. Wright and X. Ren, *J. Phys.: Condens. Matter*, 2009, **21**, 256001.

58 P. K. Gallagher, J. P. Sanders, P. M. Woodward and I. N. Lokuhewa, *J. Therm. Anal. Calorim.*, 2005, **80**, 217.

59 P. K. Gallagher, J. B. MacChesney and D. N. E. Buchanan, *J. Chem. Phys.*, 1964, **41**, 2429.

60 T. C. Gibb, *Dalton Trans.*, 1985, 1455.

61 A. Nemundry, M. Weiss, I. Gainutdinov, V. Boldyrev and R. Schollhorn, *Chem. Mater.*, 1998, **10**, 2403.

62 U. P. Muecke, K. Akiba, Anna Infortuna, Tomas Salkus, N. V. Stus and L. J. Gauckler, *Solid State Ionics*, 2008, **178**, 1762.

63 J.-C. Chen, C.-L. Chang, C.-S. Hsu and B.-H. Hwang, *Mater. Res. Bull.*, 2007, **42**, 1674.

This journal is © The Royal Society of Chemistry 2013

J. Mater. Chem. A, 2013, **1**, 11834–11841 | **11841**